Thermodynamic Structure of the Solar Corona: Tomographic Reconstructions and MHD Modeling

Diego G. Lloveras[1] · **Alberto M. Vásquez**[1,2] · **Federico A. Nuevo**[1,3] · **Cecilia Mac Cormack**[1,2] · **Nishtha Sachdeva**[4] · **Ward Manchester IV**[4] · **Bartholomeus Van der Holst**[4] · **Richard A. Frazin**[4]

Abstract Observational techniques play an essential role in advancing our understanding of the physics of the solar corona. They provide validation data

✉ D.G. Lloveras
dlloveras@iafe.uba.ar

✉ A.M. Vásquez
albert@iafe.uba.ar

✉ F.A. Nuevo
federico@iafe.uba.ar

✉ C. Mac Cormack
cmaccormack@iafe.uba.ar

✉ N. Sachdeva
nishthas@umich.edu

✉ W. Manchester IV
chipm@umich.edu

✉ B. Van der Holst
bartvand@umich.edu

✉ R.A. Frazin
rfrazin@umich.edu

[1]   Instituto de Astronomía y Física del Espacio (IAFE), CONICET-UBA, CC 67 - Suc 28, (C1428ZAA) Ciudad Autónoma de Buenos Aires, Argentina

[2]   Universidad Nacional de Tres de Febrero (UNTREF). Departamento de Ciencia y Tecnología, Sáenz Peña, Argentina.

[3]   Ciclo Básico Común (CBC), Universidad de Buenos Aires (UBA), Buenos Aires, Argentina

[4]   Department of Climate and Space Sciences and Engineering (CLaSP), University of Michigan, 2455 Hayward Street, Ann Arbor, MI 48109-2143, USA

for three-dimensional (3D) magnetohydrodynamic (MHD) models of the solar atmosphere, key to improve their space weather forecasting capabilities. Solar rotational tomography (SRT) is currently the sole observational technique that provides an empirical 3D description of some of the fundamental plasma parameters of the solar corona at a global scale. Based on EUV data of space borne instruments, SRT allows constructing 3D maps of the coronal electron density and temperature at heliocentric heights below 1.25 Rsun. We carry out a study of the corona combining tomographic reconstructions with MHD simulations using the latest version of the Alfvén Wave Solar Model (AWSoM) of the Space Weather Modeling Framework (SWMF). Target rotations were selected from the solar minimum between solar cycles (SC) 23 and 24 and the current declining phase of solar cycle 24. Tomographic reconstructions and results of the model are analyzed in distinct coronal magnetic structures. We study magnetically closed structures associated with the equatorial streamer belt, as well as magnetically open regions enclosing it. We report on the tomographic results in the different structures, their implications for the physics of the solar corona, and the current capability of the AWSoM model to reproduce the tomographic reconstructions in different regions.

Keywords: Solar Cycle, Observations; Corona,E; Corona, Structures

1. Introduction

Being the place where the solar atmosphere is heated and the solar wind accelerated, and where impulsive events such as solar flares and coronal mass ejections are energized, observation and modeling of the solar corona are tasks of great relevance to improve our understanding of the Sun-Earth environment. To advance our knowledge of the physics of the solar corona, as well as to improve its three-dimensional (3D) models, information derived from observational data plays a key role. Solar rotational tomography is currently the sole observational technique able to provide a quantitative empirical description of the 3D distribution of some fundamental plasma parameters of the solar corona at a global scale.

NOTE: Here we will put in a couple of paragraphs summarizing what SRT and DEMT are, including references and defining the accronyms in the process. We should refer to minima in particular. We should mention the instruments and missions we use as data for DEMT, and define their accronyms too. Also, a couple of paragraphs on the AWSoM model and the SWMF, including references and defining the accronyms in the process.

2. Methodology

2.1. DEMT reconstructions

NOTE: This section will summarize DEMT's main aspects and equations, only those needed to understand the paper. Nothing not needed to read this paper is

To perform the comparison two specific rotations were selected, CR-2082 (2009, 05 April through 03 May), a deep minimum period between solar cycles (SCs) 23 and 24 characterized by virtually no ARs, and CR-2208 (2018, 02 September through 29 September), a rotation during the early declining fase of SC 24.

To determine the thermodynamical structure of both rotations, the DEMT technique was applied to respective time series of EUV images covering each first half rotation. To study CR-2082 and CR-2208 data taken by the EUVI/STEREO and AIA/SDO instruments was used, respectively.

In DEMT, the low corona in the height range 1.0 to $1.25\,\mathrm{R_\odot}$ is discretized in a spherical computational grid. The size of the tomographic cell (or voxel) is set to $0.01\ \mathrm{R_\odot}$ in the radial direction, while is set $2°$ in both the latitudinal and longitudinal directions. We carried out a reconstruction using half of a solar rotation blocking the lines-of-sight comming from the disk (i.e. only using off-limb data). With this angular resolution one image every 6 hours is the cadence needed to fully constrain the inversion problem, for a total of about 55 images to cover a half solar rotation. We refer the reader to Frazin, Vásquez, and Kamalabadi (2009) for a detailed description of the technique, and to Vásquez (2016) for a recent review on all published work based on it. Here we summarize the key points. The technique involves two consecutive procedures.

creo que es la primera vez que exploramos con hollow, vale la pena explicar la diferencia en detalle?

In a first step, the time series of EUV images is used to solve a SRT problem, for each EUV band independently. As a result, the 3D distribution of the so called filter band emissivity (FBE) is determined for each band separately. The FBE, an emissivity-type quantity, is defined as the wavelength integral of the coronal EUV spectral emissivity and the telescope's passband function of each EUV channel. Line-of-sight (LOS) integration of the FBE provides synthetic images that can be quantitatively compared to the real data in the time series. To find the FBE, the tomographic problem is posed a global optimization problem in which the quadratic norm of the difference between all pairs of synthetic and real images is minimized. Spatial regularization terms are also included in the objective function as to minimize high frequency spurious artifacts that are due to the specific characteristics of the SRT sparse projection matrix (Frazin, Vásquez, and Kamalabadi, 2009; Frazin, 2000). Due to optical depth issues that may affect LOSs passing very close to the limb, and to the decay of intensity

with radii, the 3D maps produced by DEMT analysis typically cover the height range 1.02 to 1.23 R$_\odot$ (Frazin, Vásquez, and Kamalabadi, 2009).

In a second step, the FBE values obtained for all bands in each voxel are used to constrain the determination of a local differential emission measure (LDEM) distribution, which describes the temperature distribution of the electron plasma contained in each individual tomographic grid voxel. Specifically, at each tomographic voxel i, the FBE of the band k is related to the LDEM of the voxel according to

$$\mathrm{FBE}_i^{(k)} = \int \mathrm{d}T\, \mathrm{LDEM}_i(T)\, \mathrm{TRF}^{(k)}(T), \quad k = 1, ..., K \tag{1}$$

Due to unresolved coronal dynamics, tomographic reconstructions exhibit negative values of the reconstructed FBE, or zero when the solution is constrained to positive values (Frazin, 2000; Frazin, Vásquez, and Kamalabadi, 2009). These non-reconstructed voxels are indicated as black voxels in the Carrington maps of the reconstructed DEMT reults in Section 3.

Once the LDEM is determined at each voxel, the average squared electron density $\langle N_\mathrm{e}^2 \rangle$ and the electron mean temperature T_m in the voxel can be computed by taking its zeroth and first moments over temperature. More specifically, at the i-th voxel,

$$N_{\mathrm{m},i}^2 = \langle N_\mathrm{e}^2 \rangle_i \;=\; \int \mathrm{d}T\, \mathrm{LDEM}_i(T), \tag{2}$$

$$T_{\mathrm{m},i} = \langle T_\mathrm{e} \rangle_i \;=\; \frac{1}{\langle N_\mathrm{e}^2 \rangle_i} \int \mathrm{d}T\, T\, \mathrm{LDEM}_i(T), \tag{3}$$

We define next a measure of the accuracy of the LDEM model to predict the tomographic FBEs in each voxel, as

$$R_i \;\equiv\; (1/K) \sum_{k=1}^{K} \left| 1 - \mathrm{FBE}_{i,\mathrm{syn}}^{(k)} / \mathrm{FBE}_{i,\mathrm{tom}}^{(k)} \right|, \tag{4}$$

being the average relative difference between the tomographic and the synthetic FBEs. The final product of DEMT is in the form of 3D maps of the electron density and mean temperature. These relationships were derived in detail in Frazin, Vásquez, and Kamalabadi 2009 (see Appendix C).

Aclarar que consideramos Ne como $\sqrt{<N_\mathrm{e}^2>}$. ALBERT: Yo creo que es mejor hablar de $\sqrt{N_\mathrm{m}^2}$ DEMT has been improved since the previously published work. We now perform hollow-tomography with the EUV images, (definir hollow-tom) and a 3D regularized of the solution was applyed to obtain smother and more reliable result at the edge of the tomographic grid. NOTE: NOTA de Albert: Explicá que hacés sin justificarte. Luego aclará como se hizo eso en trabajos previos, y cual es el impacto esperado. Puedo proveer un párrafo de ejemplo, pero creo que será mejor que vos escribas como te salga y yo luego edito. Algo muy importante para todo el paper: proponete escribir "párrafos modulares". Es decir

que, con las razonables limitaciones, puedan moverse de lugar, de orden, y sigan funcionando. No definiría hollow-tomography, es un término coloquial interno nuestro. Lo correcto es que al hablar de datos mucho más arribas expliques que los datos del disco no se utilizan, pero no le des un nombre a la tomografía.

2.2. AWSoM simulations

NOTE: This section will summarize the AWSoM model. After a first version is written we will surely require some input from the Michigan friends. Points to cover:

- Data input. Link with the data input for DEMT in terms of dates, etc. One paragraph.
- Main physical and technical aspects (grid in particular) of the model. One paragraph.
- Explain the artificially extended TR. One paragraph.
- What are the products of the model we care about in this paper. One paragraph.

In the transition region (TR), the plasma heats up and becomes less dense by several orders of magnitude over a short distance. Modeling this region realistically has a very high computational cost. For this reason, the model uses an artificially extended TR about $\approx 0.05\,\mathrm{R_\odot}$ thick, as well as artificially large values for the electronic density and temperature as boundary conditions in $r = 1\,\mathrm{R_\odot}$. Consequently, model results below $\approx 1.05\,\mathrm{R_\odot}$ were not taken into account in this article.

2.3. Tracing of results along fieldlines

NOTE: This section will explain how the AWSoM magnetic model is used to trace the thermodynamic products of both DEMT and AWSoM along the fieldlines of AWSoM. This requires covering the following points:

- A first paragraph qualitatively describing the process. This includes mentioning that the AWSoM products are first interpolated into the DEMT grid.
- A short paragraph describing the numerical method used to trace field lines. We have a nice version of this in your previous paper. At this point the reader should understand that for each field line we have its geometry $\mathbf{r}(s)$ as a function of the distance s along the loop, with $s(1\,\mathrm{R_\odot}) \equiv 0$.
- Explain very simply how then that for each voxel the middle point of the field line is selected and assigned the DEMT and AWSoM products of that cell. At this point the reader should understand that for each field line we have: $Q[r(s)]$, where Q is any given quantity from either the DEMT model (specifically $\sqrt{N_\mathrm{m}^2}$ and T_m) or the AWSoM model (specifically N_e and T_e).
- Explain fits to the DEMT results $\sqrt{N_\mathrm{m}^2}(r)$, $T_\mathrm{m}(r)$.
- Explain then the classification of field lines.

For both rotations, the DEMT and AWSoM 3D maps of electron density N_e, electron mean temperature T_m and electron temperature T_e respectively were traced along the magnetic field lines modeled using AWSoM as described at the end of Section 2.1. In the case of closed loops, results were separated into their two legs, defined as the two segments that go from the coronal base up to the apex.

For each open field line, and for each leg of the closed ones, an exponential fit was then applied to the $\sqrt{N_\mathrm{m}^2}(r)$ data points, and a linear fit applied to the $T_\mathrm{m}(r)$ data points, as described by

$$\sqrt{N_\mathrm{m}^2} \ = \ N_0 \, \exp\left[-\left(h/\lambda_\mathrm{N}\right) / \left(r/\mathrm{R}_\odot\right)\right] \tag{5}$$

$$T_\mathrm{m} \ = \ T_0 \, + \, m\,h \tag{6}$$

where $h \equiv r - 1\,\mathrm{R}_\odot$ is the coronal height measured from the photosphere. In the electron density fit, $\lambda_\mathrm{N}\,[\mathrm{R}_\odot]$ is the density scale height and $N_0\,[\mathrm{cm}^{-3}]$ is the electron density at the footpoint ($h = 0$) of the loop. In the electron temperature fit, $m\,[\mathrm{MK/R}_\odot]$ is the slope and $T_0\,[\mathrm{MK}]$ is the electron temperature at the footpoint of the loop. The slope m is the radial gradient of the electron temperature along the loop, which we denote as $m = \nabla_r T_\mathrm{m}$ hereafter, being $\nabla_r \equiv \mathbf{e}_r \cdot \nabla$ the radial derivative operator, where $\mathbf{e}_r$ is the heliocentric radial unit vector.

In the case of the electron density, the fitted function corresponds to the isothermal hydrostatic equilibrium solution, allowing for variation of the solar gravitational acceleration with height. This choice of function provides a straightforward means to directly evaluate how compatible is the observed coronal thermodynamical state with the hydrostatic solution.

In the present work we focus on lines with increasing and decreasing temperatures in linear form. In other words, we selected those legs where the Pearson correlation coefficient ρ between temperature T and radius r meets $|\rho(T,r)| > 0.5$. (with p-value less than 0.05). In this way, those legs in which the DEMT results cannot ensure a noticeable change in temperature between the base and the apex, are discarded.

The linear fit allows characterization of its variation with height by means of a characteristic temperature gradient $\nabla_r T_\mathrm{m}\,[\mathrm{MK/R}_\odot]$ along each leg. En realidad esta regresion lineal utiliza de por si los errores, pero luego tmb los uso para el test de hipotesis, quizas vale la pena ponerlo solo ahi.

To measure how good the quality of the exponential fit to the electron density and the linear fit to the temperature data are, a chi-square merit function was used (see Section 15.2 Press *et al.* (2002)). The errors were estimated in Lloveras *et al.* (2017), 0.07 MK for T_m and $4.0\,10^6 cm^{-3}$ for N_e and legs with p-value > 0.005 were rejected.

To be selected a leg must meet all following conditions.

i) The leg must go through at least five tomographic grid cells with reconstructed data, and there must be at least one data point in each third of the range of heights spanned by the leg.

ii) The value of the Pearson correlation coefficient meets $|\rho(T,r)| > 0.5$.

iii) The p-value of both the exponential and linear fit must be less than 0.05.

For the two targeted rotations, DEMT and AWSoM results were traced along the AWSoM field lines, which provides a way to characterize the global thermodynamic state of the inner solar corona and to compare them. To that end four different types of legs corresponding with four different types of magnetic structures were selected:

- Type 0 - Small (meaning with apex within the DEMT range of heights) closed field lines in the latitudes range $[-30°, +30°]$ and $\nabla_r T_{\mathrm{m}} < 0$.
- Type I - Small closed field lines in all latitudes, with $\nabla_r T_{\mathrm{m}} > 0$.
- Type II - Large closed field lines (meaning their apex surpasses the DEMT range of heights) in the latitudes range $[-90°, -30°] \cup [+30°, +90°]$ and $\nabla_r T_{\mathrm{m}} > 0$.
- Type III - Open field lines (meaning with apex out the DEMT range of heights) in the latitudes range $[-90°, -60°] \cup [+60°, +90°]$ and $\nabla_r T_{\mathrm{m}} > 0$.

Hice las definiciones con gradiente de temperatura para que quede mas claro, pero en realidad uso el pearson. NOTE: Charlemos los tres en persona de esto.

2.4. Energy input flux

NOTE: This section will summarize how loop integrated energy quantities are computed from the DEMT products and the AWSoM magetic model alone. The summary will not include any derivation and will refer to Cecilia's paper. Only the results that are relevant are to be explicited. Start by explaining the model and assumptions, and end up summarizing the loop-integrated products (radiative and conductive fluxes). At the end the reader should understand that their sum is the enery input flux required at the coronal base to maintain the loop stable. This should be a very short section, as it is a summary of one previous paper alone.

Due the difference between temperatures of transition region and solar corona, there must to be a heating mechanism that compensate all the losses present in the atmosphere and maintain stable the plasma temperature. Previous works have studied this mechanism by observations and modeling, but mostly for active regions. Mac Cormack *et al.* (2017) have developed a technique that estimate the heating injected into the loops during a period of minima activity. Using DEMT combined with an extrapolation of magnetic field, as we detailed before, they obtain the different plasma parameters along each magnetic loop, and therefore, compute the energy input flux required to maintain them stable. The model assume a simple energy balance for each magnetic flux tube, where the losses by radiative power (E_r) and thermal conduction power (E_c) are compensated by some coronal heating power(E_h) (Aschwanden, 2004):

$$E_h(s) = E_r(s) + E_c(s), \tag{7}$$

where s is the position along each magnetic flux tube and the powers are in units of $[\mathrm{erg\,sec^{-1}\,cm^{-3}}]$.

NOTE: Trabajé todo lo naranja. Primero decidí que es mejor no numerar E_c sino F_c. Eso te quedará claro cuando agregues las ecuaciones (11) y (12) que te indico más abajo y leas el último párrafo naranja de abajo, ahí cierra todo. Además describí que son los ϕ en forma correcta. El texto previo estaba muy flojón, entre otras cosas se hablaba de una (inexistente) "conductive loss function" y de una (incorrectamente denominada) "area along the loop". Obviamente luego de chequear este texto naranja borrá esta nota azul en particular.

The thermal conduction power E_c equals the divergence of the conductive heat flux F_c, i.e. $E_c(s) = [1/A(s)] \, \mathrm{d}[A(s) \, F_c(s)]/\mathrm{d}s$, where $A(s)$ is the transversal area of the magnetic flux tube at position s. Under a quiescent solar corona plasma regime, the conductive flux is assumed to be dominated by the electron thermal conduction, described by the usual Spitzer model (Spitzer, 1962)

$$ F_c(s) = -\kappa_0 \, T(s)^{5/2} \, \frac{dT}{ds}(s), \tag{8} $$

where $\kappa_0 = 9.2 \times 10^{-7} \mathrm{erg\, sec^{-1}\, K^{-7/2}}$ is the Spitzer thermal conductivity.

Radiative power depends on the amount of plasma in certain temperatures that can radiate. The model estimate it by integrating the squared density multiplied by a radiative loss function $\Lambda(T)$. This function depends on plasma temperature and is calculated by the atomic database and the plasma emission model from CHIANTI (Del Zanna *et al.*, 2015). Then, the expression for radiative power obtained is:

$$ E_r = \int \mathrm{d}T \, \mathrm{LDEM}(T) \, \Lambda(T) \tag{9} $$

The energy balance given by Equation (7) is then integrated in the volume of any given coronal magnetic flux tube. Dividing the result by the flux tube area at the coronal base, and making use of the soleidonal conditon of the magnetic field, a field-line integrated version of that energy balance is found,

$$ \phi_h = \phi_r + \phi_c. \tag{10} $$

where the line integrated flux quantities $\phi_{r,c}$ $[\mathrm{erg\, sec^{-1}\, cm^{-2}}]$ are given by (Mac Cormack *et al.*, 2017),

$$ \phi_r = \left(\frac{B_0 \, B_L}{B_0 + B_L} \right) \int_0^L ds \, \frac{E_r(s)}{B(s)} \tag{11} $$

$$ \phi_c = \left(\frac{B_0 \, F_{c,L} - B_L \, F_{c,0}}{B_0 + B_L} \right) \tag{12} $$

Note that, for any given field line, all quantities in these two expresions can be computed from the DEMT and AWSoM models through Equations (8)-(9). Once computed, the quantity ϕ_h can be calculated, which is the energy input flux required at the coronal base of each coronal field-line to mantain a stable coronal structure.

3. Results

3.1. Tomographic Results

NOTE: This section will show first the DEMT products in the form of Carrington maps at three heights, for the two target rotations. It will then show the latitude/longitude location of the four types of magnetic loops (defined in Section 2.3) at a sample height. Then, for the each type of loop, we will show histograms of the values of different DEMT products traced along them, charerizing in a quantitative fashion the DEMT results in distinct magnetic structures. It will also include a quantitative comparison between the two target rotations of the median values of the DEMT products in each type of loop.

To perform a comparative study of the thermodynamic structure of the inner corona in different solar cycles we carry out a DEMT reconstruction for two rotations: CR-2082, using STEREO/EUVI data and CR-2208, using SDO/AIA data. Once the LDEM was determined for each rotation, the square root of the mean value of the electron density squared $\sqrt{N_m^2}$ and the electron mean temperature T_m were computed at each voxel of the tomographic computational grid by means of Equations 2 and 3. As an example, Figures 1 and 2 show the latitude-longitude maps of DEMT results for both rotations at three different heights of interest. The lowest height where the tomography gives results, the lowest height where the AWSoM model results are reliable and a representative average height were selected, that is $r =1.025$, 1.065 and 1.105, $R_\odot$ respectively. Black voxels correspond to non-reconstructed voxels (explained in Section 2.1). Thick-black curve indicates the magnetic open/closed boundary based on the magnetic field of AWSoM model.

While CR-2082 was highly axisymmetric and showed two ARs (active region) in latitude $+30°$ and longitude $50°$ and $120°$. CR-2208 showed two AR, one around latitude $+5°$ and longitude $140°$ and the other around latitude-longitud $+5°$, $300°$. Except for these ARs, in both rotations the open-closed boundaries derived from the respective AWSoM model match the shape of the contour levels of the tomographic maps of both the electron density and the electron mean temperature. In the AR, there is a lack of match between the open-closed boundaries and the tomographic reconstructions of density and temperature, that is why those ranges were excluded from the analysis.

PARRAFO CORTO DE OBSERVACIONES QUE LUEGO SERAN CORROBORADAS CON HISTOGRAMAS. A visual inspection of Figures 2 and 3 suggest/indicates that the streamer region of CR-2082 was denser and colder than CR-2208. In both rotations, but specifically in CR-2082 the temperature in the equatorial latitudes tend to decrease with height while the latitudes between the open-close boundaries and the equatorial latitudes tend to increase. These thermodynamic structures have been reported for other rotations in previous works (Lloveras *et al.*, 2017). Closed regions are characterized by relatively larger values of density and temperature in comparison to the open regions. que mas se puede agregar?

To study the variation of the DEMT results in different magnetic structures we traced $\sqrt{N_m^2}$ and T_m along the magnetic field lines of the AWSoM model.
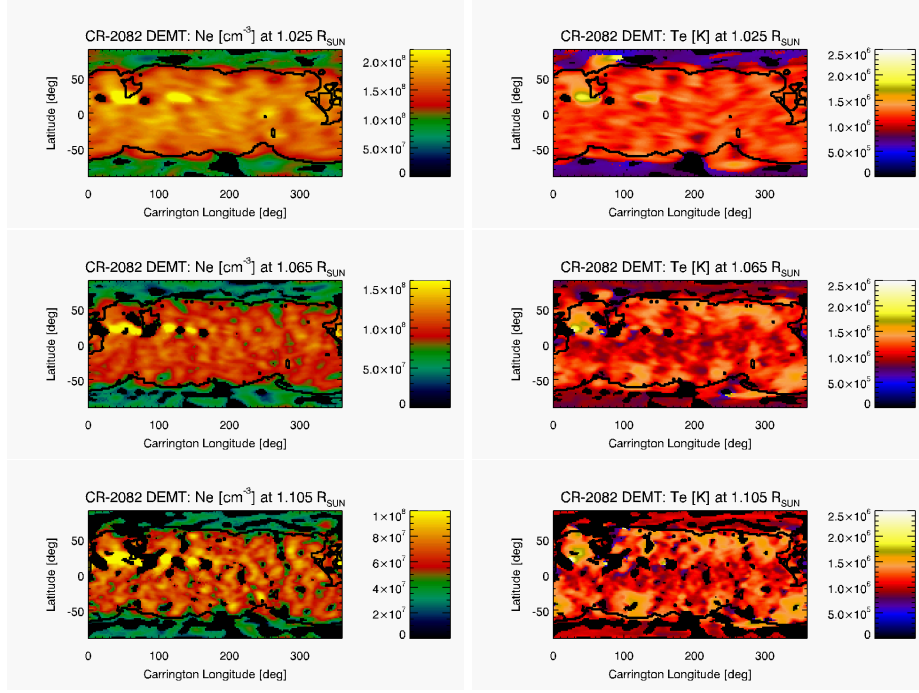
Figure 1. Carrington maps of DEMT products $\sqrt{N_{\mathrm{m}}^2}$ (left panels) and T_{m} (right panels) for CR-2082. Top, middle and bottom panels show the results at three heliocentric heights, 1.025, 1.065 and 1.105 $\mathrm{R}_\odot$ respectively. Black voxels correspond to non-reconstructed regions (see text in Section 3.1) and thick-black curves indicate the open/closed boundaries.

For both rotations, all field lines that meet the criteria listed in Section 2.3 were selected. For each field line, the data points of electron density and electron mean temperature as a function of height were fitted to the Equations 5 and 6.

As a result, the electron density $N_0(r = 1.0\,\mathrm{R}_\odot)$ and scale height λ_N were computed for each leg, as well as the temperature gradient $\nabla_r T_{\mathrm{m}}$, and the height-averaged (along the leg) electron temperature $\langle T_{\mathrm{m}} \rangle$. As the DEMT technique studies only coronal conditions, *i.e.* above height $r \approx 1.025\,\mathrm{R}_\odot$, the exponential fit to the electron density data as a function of height may be used to compute the tomographic electron density at the coronal base $\sqrt{N_{\mathrm{m}}^2}(r = 1.025\,\mathrm{R}_\odot)$ as in previous articles. In this case, for further comparison analysis with the AWSoM results, we selected the lowest height where the results of the MHD model are reliable, that is $1,055\,\mathrm{R}_\odot$.

As a way of knowing the physical position of all traced lines, Figure 4 shows the latitudinal-longitudinal location of all open and closed file lines traced in gray scale at $1.105\,\mathrm{R}_\odot$ for both rotations, where the ARs where excluded. At top, all traced legs with enaugh tomographic data are shown. In black all legs corresponding to closed lines and in grey corresponding to open lines. This traced lines were divided into four types as explained in Section 2.3 and the fit in density and temperature was applied, selecting only those legs that met the criteria.

Figure 2. Same as Figure 1 but for CR-2208.

Of the 45000 legs selected in 2082, 14% are type 0, 38% are type I, 23% are type II and 25% type III, on the other hand of the 59000 legs selected in 2208, 8% are type 0, 43% are type I, 22% are type II and 30% type III.

This selection of types of lines automatically leads to specific regions arranged along all longitudes associated with different thermodynamic, with good symmetry between both hemispheres in both rotations.

To compare obtained traced results in both rotations and for each type of lines (associated with differents types of regions), Figure 5 shows histograms (normalized to the total amount of the field lines selected) of the temperature radial gradients ($\nabla_r T_\mathrm{m}$). The lack of population around values close to zero is due to the requirement $|\rho_t| > 0.5$ which discards quasi-isothermal legs.
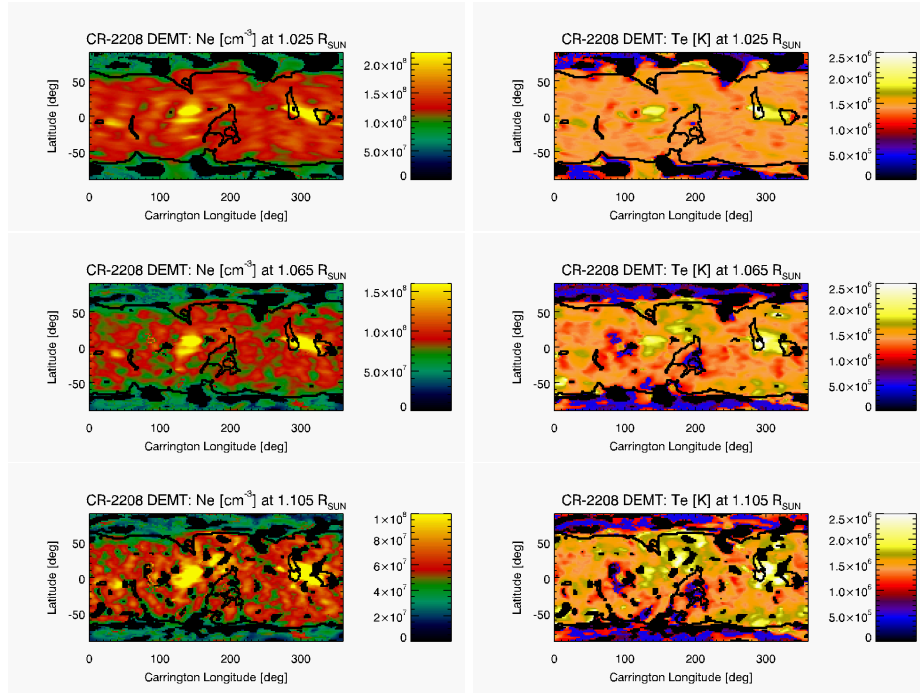
Figure 3. Carrington maps of the measure R defined by Equation (4), for CR2082 (left panels) and CR2208 (right panels), at heights 1.025, 1.065 and 1.105 R$_\odot$, from top to bottom. NOTE: Aquí deberían ir los seis mapas de R correspondientes. Quizá los saquemos, pero a esta altura es importante que los veamos nosotros para evaluar la precisión de predicción de las reconstrucciones de los resultados LDEM en la zona abierta. Quizá terminemos haciendo el comentario adecuado y sacamos la Figura, o quizá la dejamos, pero veamos esa info aquí. Noten el cambio en NARANJA que hice en torno de la Ecuación (4) más adelante.

Both rotations are characterized by lines of type 0 with mean values of $-2.5\,\mathrm{MK/R_\odot}$, mean values of $2.3\,\mathrm{MK/R_\odot}$ in type I and $2.4\,\mathrm{MK/R_\odot}$ in type II. The only notable difference is the smaller number of type 0 lines in CR-2208 and the mean value of $4.5\,\mathrm{MK/R_\odot}$ in type III for CR-2208 which is twice that for the other rotation.

As an example of the traced magnitudes, Figure 6 shows the statistical results of both rotations for all field lines types. From top to bottom type 0 to type III. From left to right the panels show the statistical distribution of $N_{\mathrm{CB}} \equiv \sqrt{N_{\mathrm{m}}^2}(r = 1.055)$, λ_N, $\langle T_{\mathrm{m}}\rangle$, in each panel the median m is indicated.

For all type of lines, Table 1 summarize the quantitative comparative analysis between the results of the two target rotations sampling both minima. For CR-2082 quantities are expressed as absolute values, qhile for CR-2208 they are informed relative to the corresponding results for CR-2082. The following major results concerning the structure of each rotation individually and their comparison can be drawn.

si queda una asociacion directa entre los tipos de lineas y las estructuras de streamer, CH etc entonces usaria esos nombres a continuacion.
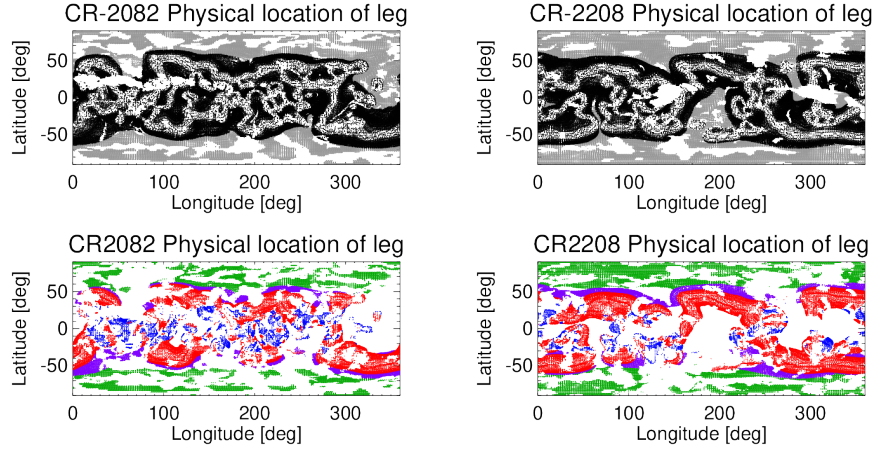
Figure 4. *Top panels:* latitude-longitude location at heliocentric height $r = 1.105\,\mathrm{R}_\odot$ of all open (grey) and closed (black) traced field lines for which there are along at least five DEMT data points, for both CR2082 (left) and CR2208 (right). *Bottom panels:* latitude-longitude location (at the same height) of each traced leg that meets the criteria listed in Section 2.3. Type 0, I, II and III legs (see text) are shown in blue, red, violet and green, respectively, for CR-2082 (left) and CR-2208 (right).
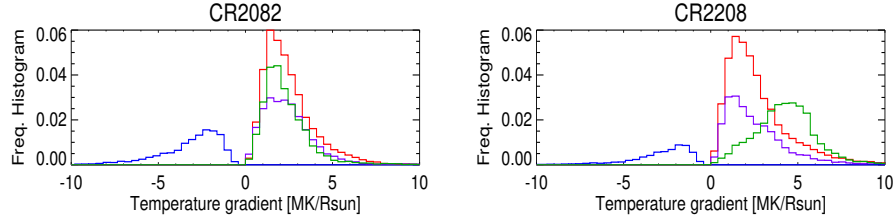

Figure 5. Frequency histograms of the temperature radial gradient for the different four types of legs shown in Figure 4 (using the same color code) for CR-2082 (left panel) and CR-2208 (right panel).

From the equatorial streamer of both rotations, increasing latitudes show decreasing coronal base density, and increasing density scale height and electron temperature. In both rotations the CH regions are characterized sub-MK temperatures, and coronal base densities of order $\approx 1/2$ of the equatorial streamer. Histograms with sharp populations indicates that for both rotations the values of all physical quantities exhibit a strong symmetry between both hemispheres.

A comparison of the results between the two rotations shows that CR-2208 is characterized by lower values (between 11% and 16%) of coronal base electron density than CR-2082, higher values of density scale height (between 4% and 19%) and higher values of electron temperature (between 6% and 21%).

To compare integrated quantities along loops, we select those close loops where both legs meet the requirements of Section 2.3. In an analogous way to the legs definition, we will refer to them as loops of type 0, I or II to those whose
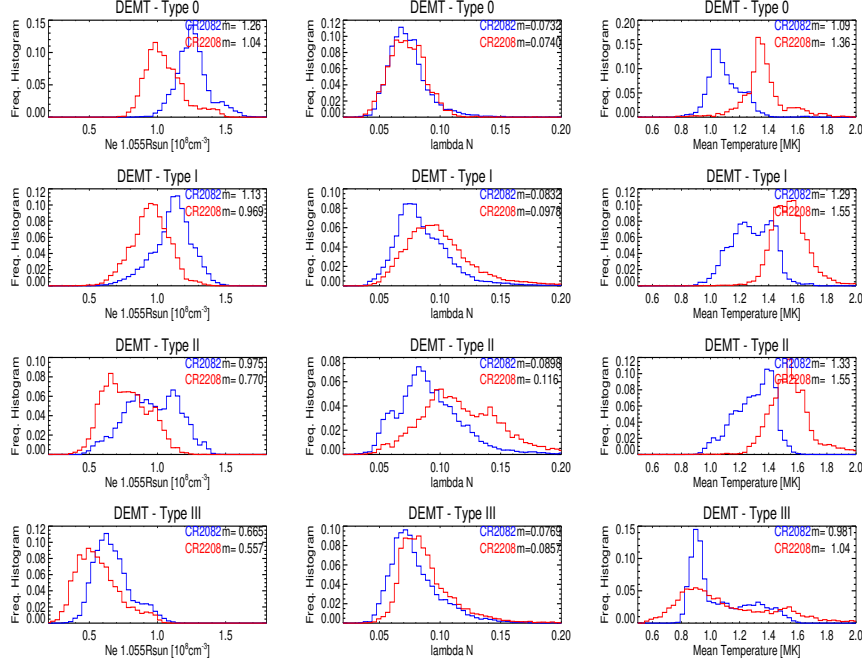
Figure 6. Statistical distribution of DEMT results traced along legs of type 0, I, II and III (from top to bottom), as defined in Section 2.3. From left to right: electron density at the coronal base $N_{\mathrm{CB}} \equiv \sqrt{N_{\mathrm{m}}^2}(r = 1.055\,\mathrm{R}_\odot)$, electron density scale height λ_N, and loop-averaged electron temperature $\langle T_{\mathrm{m}}\rangle$. Results for target rotations CR2082 and CR2208 are shown in blue and red color, respectively. In each panel the median value m is indicated. NOTE: (by Albert) The histogram Figures in this draft need to be improved, in particular font size-and-type need to be optimized for clear reading. Also, we need to improve their X/Y ratio, here I stretched the Y size a bit in the LaTeX source.

both legs meeting the criteria. When two legs of the same loop have a decreasing temperature with height (type 0), they are called down loops.

For both target rotations, and for loops of type 0, I and II, Figure 7 shows the frequency histogram of the loop-integrated energy flux quantities ϕ_h, ϕ_r and ϕ_c in green, blue and red color, respectively.

Type 0 loops present slightly larger gradients than type I. Therefore, type 0 present bigger amount, in modulus, of loop-integrated conductive flux. Due conductive flux negative can not be assumed as a loss but it can be contributing to the coronal heating. Thus, to compensate the radiative losses, a lower loop-integrated energy input flux (ϕ_h) is required.

We can see, on type 0 loops, a median value of energy input flux for CR2082 twice bigger than CR2208. Also, in both rotations, we observe a negative population of loop integrated energy input flux. This can refer to some loops where loop-integrated radiative flux is too small in comparison with the larger gradients of negative conductive flux, resulting in negative energy input flux.

The type I loops show a loop-integrated positive conductive for each loop in both rotations consistent with positive gradients of temperatures. The conduc-

Table 1. Median value (indicated as "Md") of the statistical distribution of N_{CB}, λ_N, and $\langle T_{\mathrm{m}}\rangle$ for each coronal type of lines defined in Section 2.3. For CR-2082 values are expressed in absolute terms, while for CR-2208 they are informed as a percentual variation relative to the CR-2082 value. *Propongo que para todas las cantidades absolutas informes siempre dos cifras significativas, y que todos los porcentajes los redondee a cero decimales (o sea, a veces una y a veces dos cifras significativas) y que no uses puntos para estos nunca. Doy dos ejemplos para no dejar dudas. Para N_{CB} de Type-II: 1.0 (−21%). Para $\langle T_{\mathrm{m}}\rangle$ de Type-III: 1.0 (+6%).*

Type	Md(N_{CB}) [$10^8\,\mathrm{cm}^{-3}$]	Md(λ_N) [$10^{-2}\,\mathrm{R}_\odot$]	Md($\langle T_{\mathrm{m}}\rangle$) [MK]
0	1.26 (−17.4%)	7.3 (+13.6%)	1.09 (+24.7%)
I	1.13 (−14.1%)	8.3 (+18.1%)	1.29 (+20.1%)
II	0.97 (−20.6%)	8.9 (+29.1%)	1.33 (+16.5%)
III	0.66 (−16.2%)	7.7 (+11.4%)	0.98 (+ 6.1%)

tive flux have values around $0.3\ 10^5 [\mathrm{erg\ sec^{-1}\ cm^{-2}}]$ in both rotations. Similar results have been found for loop-integrated radiative flux and energy input flux for both rotations.

No son los mismos colores que el paper de ceci, tmb quizas podriamos poner la cant de LOOPS y los valores medianos, ceci insiste.

3.2. Tomography and Models

NOTE: This section will show the results of AWSoM for N_e and T_e, and how they compare with the corresponding results of DEMT ($\sqrt{N_{\mathrm{m}}^2}$ and T_{m}). It will first show the Carrington maps of N_e and T_e at the same three heights we showed the same maps for the DEMT results. Then it will show the lat/lon location of loops of type I, II and III at a middle height, just loke for DEMT results. As the two targets are highly axis-symmetric, a first quantitative comparison between AWSoM and DEMT will be shown as longitude-averaged latitudinal profiles of the results of both models at a sample height. To make comparisons in distinct magnetic structures, we will also show the average radial dependence of results for loops of type I, II and III, overplotting the AWSoM and the DEMT results. For the tree types of loops we will show histograms of the DEMT and AWSoM products along field lines. This is a LOT of information from which and we need to pull out a few clear conclcusions.

The thermodynamic results of AWSoM are shown in Figures 8 and 9. That is latitude-longitude maps for N_{e} and T_{e} modeled for CR-2082 and CR-2208 at $r = 1.025, 1.065$ and $1.105\,\mathrm{R}_\odot$. The black curve denotes the same open-close boundary showed in Figures 1 and 2 respectively.

A visual inspection of these maps shows that both reconstructions are very axysimmetric for N_{e} and T_{e} as well. The closed region is denser and hotter than the open region. The density and temperature gradients are maximum
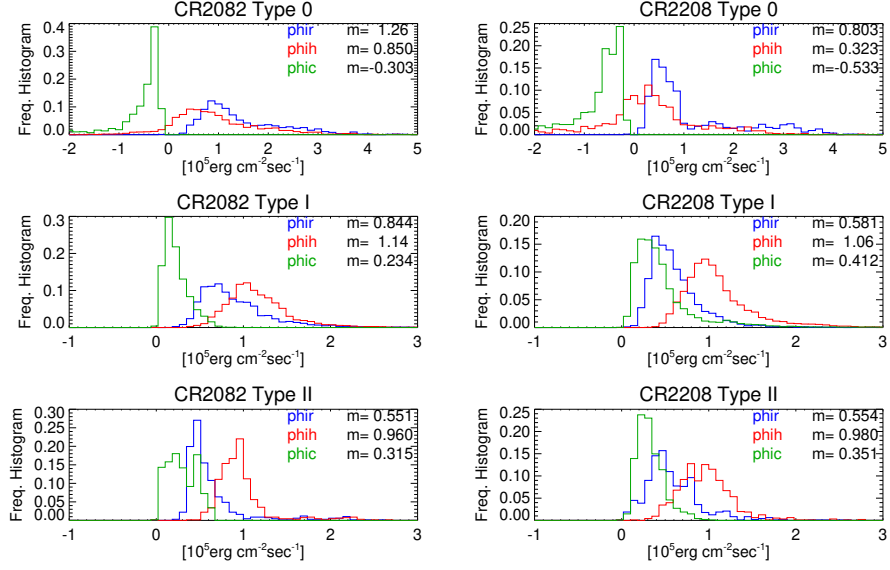
Figure 7. Statistical results of the loop-integrated energy flux quantities ϕ_r, ϕ_c, and ϕ_h in colors blue, red and green, respectively for CR-2082 (left) and CR-2208 (right). From top to bottom, panels show the results for loops of type 0, I and II, which are loops for which both legs meet the criteria from Section 2.3. NOTE: (by Albert) En el XYOUTS podés poner la letra griega ϕ usando los comandos "!4" y "!3", y para que te salga r,c,h como subíndice pero no tan pequeño usá: "!Dp!N", dónde p=r,c,h.

in the open-close boundary. The open field regions in low latitudes maintain thermodynamic values associated with open regions. The reconstruction of CR-2082 does not show clear the ARs, while CR-2208 shows a well reconstruction of both AR around latitude-longitud $+5°$, $140°$ and $+5°$, $300°$. In both rotations the open-closed boundaries derived from the AWSoM model match the shape of the contour levels of both the electron density and the electron temperature.

The same intensity scales in both density and temperature can be observed between the tomographic results and those of AWSoM in both rotations, as well as the same thermodinamic structures. That is, equatorial latitudes, mid laditudes and the open regions.

In the same way as in Section 3.1, the model results were traced along the magnetic lines obtained with it. This allowed to obtain $N_e(r)$ and $T_e(r)$ along the magnetic lines and fit them to the Equations 5 and 6.

The actual version of the AWSoM model can not reproduce down legs, so for a further comparison we only select lines of type I, II and III of those meeting the criteria described in Section 2.3.

As a way to understand the distribution of legs, Figure 10 shows the latitudinal-longitudinal location of the traced legs at top and the selected fitted legs meeting the criteria at $1.105\,\mathrm{R}_\odot$ for both rotations, in the same way as in Section 3.1. In red the type I lines, populating mostly the entire streamer. In violet the type II
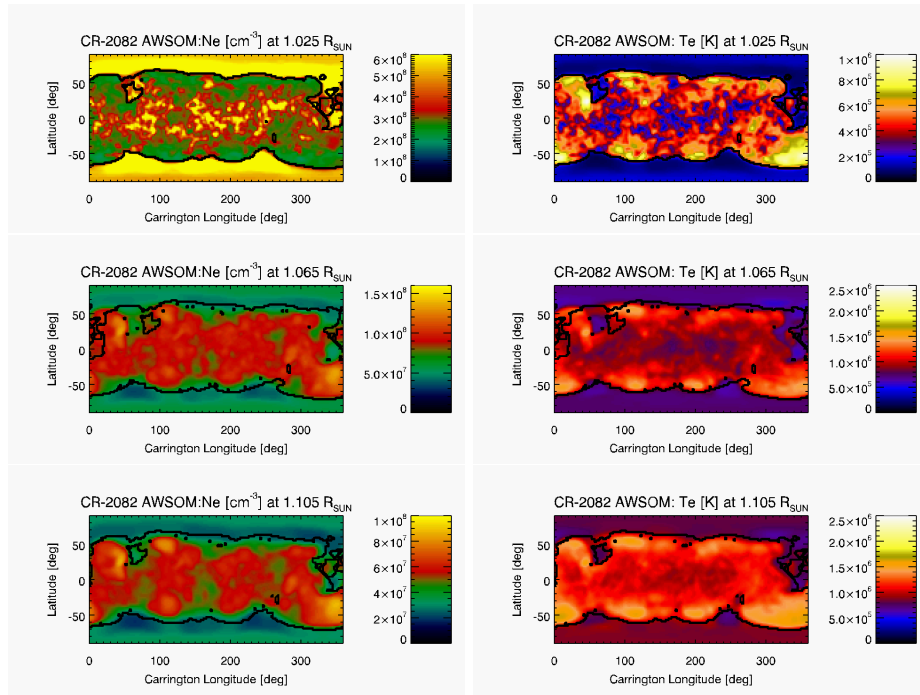
Figure 8. Carrington maps of density (left panels) and temperature (right panels) obtained with AWSoM model for the same three heights shown in Figure 1.

lines, populating the edge that assemble the envelope around the streamer, and in green dots the type III lines, populating the coronal holes.

The reader may notice that these structures are the same as those in Figure 4 but more filled. The cause is twofold, on the one hand the same magnetic model was used to trace both DEMT and AWSoM results, on the other hand is because giving the model smoother results, fewer fitted lines are filtered.

To highlight the latitudinal structures observed in Figures 1 and 8 for CR-2082 as well as Figures 2 and 9 for CR-2208, Figure 11 shows for both rotations the latitudinal variation of both the electron density and the electron mean temperature at the height $r = 1.105\,\mathrm{R_\odot}$, averaged over all longitudes (excluding the AR). DEMT results are shown in blue lines while AWSoM results in red. While the temperature shows a maximum in each hemisphere, the density has a simpler behavior, with higher values in the low-latitudes of the streamer and a nearly monotonic decrease towards larger latitudes. The vertical black lines denotes the average of the open-close boundary in both hemispheres to each rotation.

Me gustaria hacer un comentario de cierre para esta figura que refiera las Figuras 3 y 9, como la linea de abajo, y que conecte con los histogramas que vienen a continuacion. Si no queda bien, hay que mover esta figura entre la actual figura 8 y 9.
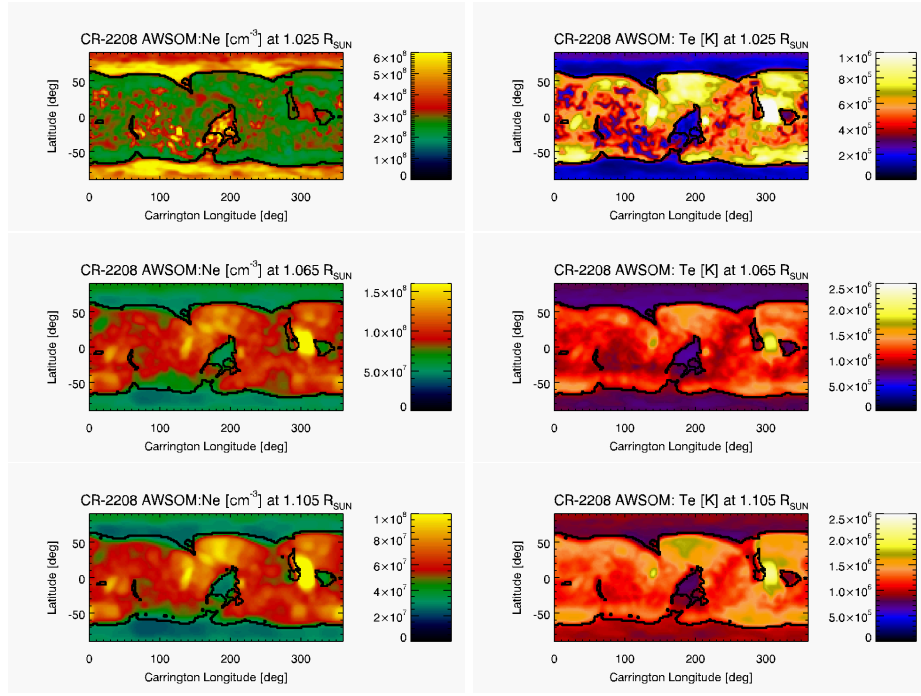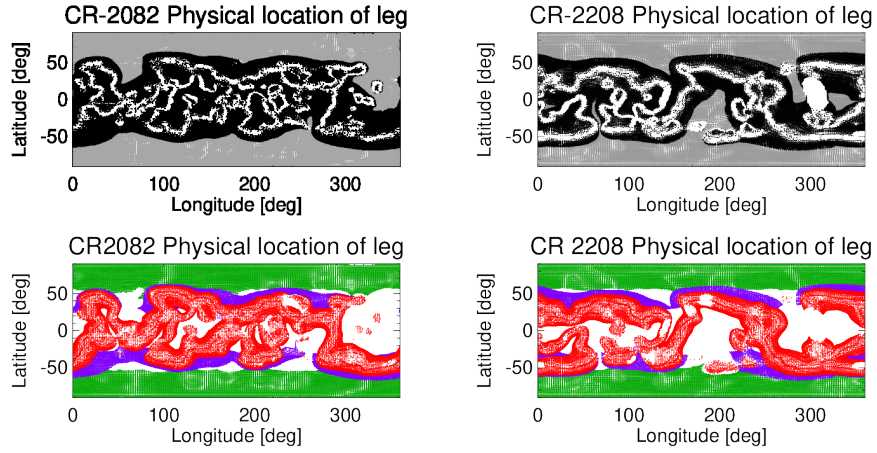
Figure 9. Same as Figure 9 for CR-2208.

Figure 10. Same as Figure 4, but using the density and temperature of the AWSoM model to classify its legs in types I, II and III. The model does not exhibit legs of type 0.

This longitude-averaged behaviors match well with the physical locations of the legs shown in Figures 10 and 4.

According to the visual inspection on the maps of carrington, the latitudinal profiles comparing both DEMT and AWSoM results are on the same scale. Little difference in density is observed in CR-2208 and in temperature in CR-2082, while DEMT in CR-2082 was 20% denser. Finally, DEMT results for CR-2208 were 25% hotter in the streamer and 30% colder in the polar zone than AWSoM. Density profiles on AWSoM show an increase around the polar zone, which seems like an artifice.
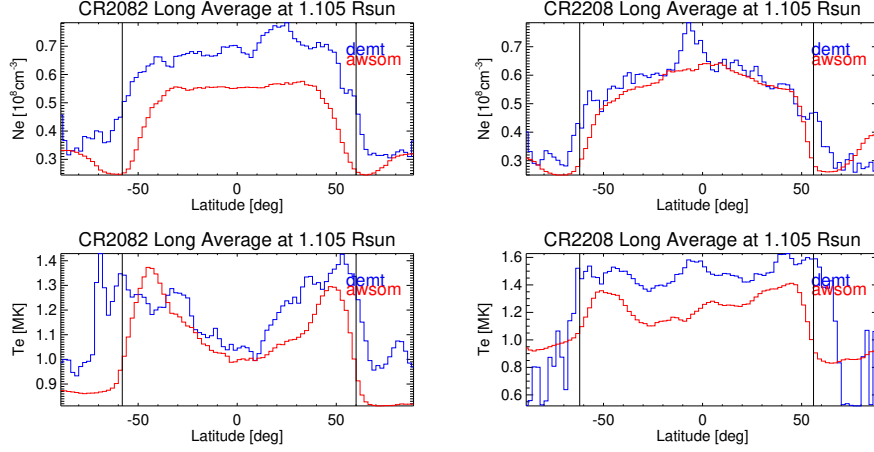

Figure 11. Longitude-averaged latitudinal dependence of the electron density (top) and temperature (bottom) for DEMT (blue) and AWSoM (red) results at $1.105\,\mathrm{R}_\odot$. The left (right) panels correspond to CR-2082 (CR2208). The vertical black line indicates the longitude-averaged latitudes of the open/close magnetic boundary in both hemispheres. NOTE: (by Albert): The idea of this Figure is to show how DEMT and AWSoM compare AS A FUNCTION OF LATITUDE at an intermediate height of the DMET grid, averaged in longitude (excluding zones with ARs).

To summarize the comparison between both results during both rotations at full height, it is shown in Figure 12 the average fits of $N_e(r)$ and $T_e(r)$ for legs of type I (blue), II (red), and III (green) for both rotations.

In average all temperature and density behavior from both results are on the same scale. The coronal base densities of AWSoM were lower than those of DEMT in CR-2082 and higher in CR-2208. The fact that the density decays to similar values between both results suggests a similar height scale. Onthe other hand basal temperature of AWSoM was lower in both rotations, but the temperature gradients are very similar en each type of legs, showing a very similar increase of temperature with height.

Tu summary the statistical comparison, Figure 13 and 14 shows the statistical results of both rotations for the three types of field lines traced with DEMT (blue) and AWSoM results (red). From left to right the panels show the statistical distribution of N_{CB}, λ_N and $\langle T_{\mathrm{m}} \rangle$. For all types of lines, Table 2 summarizes the median value of the statidtical distribution of each physical quantity derived from the analysis. The DEMT quantities are expressed as absolute values, while for ASWSoM they are informed relative to the corresponding result for DEMT.
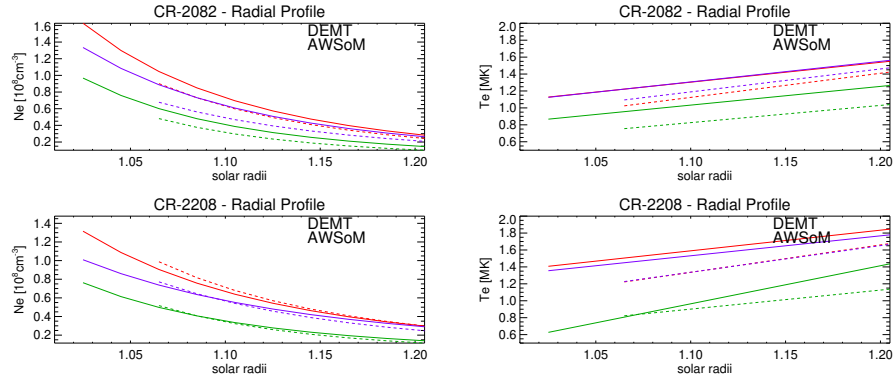
Figure 12. Average fits to $N_e(r)$ (left panels) and $T_e(r)$ (right panels) for legs of type I (red), II (violet), and III (green), for CR-2082 (top panels) and CR-2208 (bottom panels). Solid lines correspond to DEMT results while dashed lines correspond to AWSoM results. NOTE: (by Albert): The idea of this Figure is to show how DEMT and AWSoM compare AS A FUNCTION OF HEIGHT, in three distinct types of magnetic structures, and for both rotations.

aca podria ir un pequeño parrafo que resuma las diferencias. Pero justo a continuacion empiezan las conclusiones y uno tiende a repetir, no se como encararlo para que no quede dos veces lo mismo y tan pegado uno de lo otro.
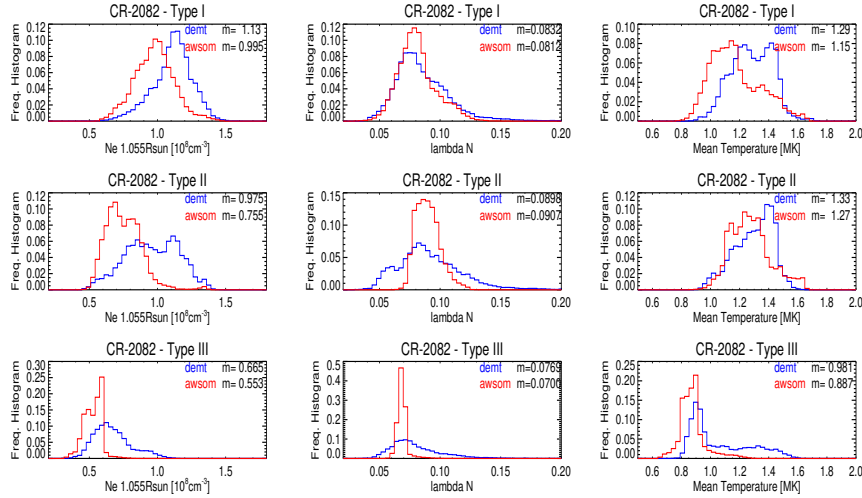

Figure 13. Statistical distribution of DEMT (blue) and AWSoM (red) results traced along legs of type I, II and III (from top to bottom), as defined in Section 2.3. From left to right: electron density at the lowest coronal height of the AWSoM model $N_e(r = 1.055\,R_\odot)$, electron density scale height λ_N, and leg-averaged electron temperature $\langle T_m \rangle$. In each panel the median value m is indicated.
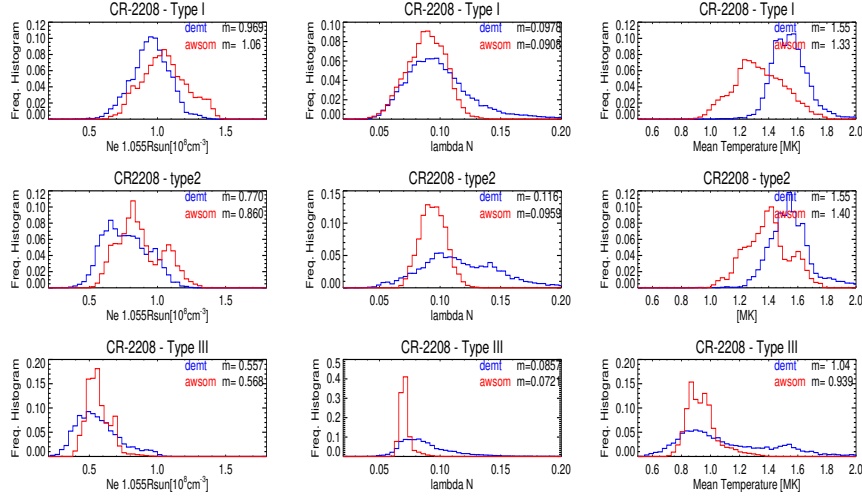
Figure 14. Same as Figure 13 for CR-2208.

Figure 15 show the longitude-averaged AWSoM radial wind speed V_r at $6\,\mathrm{R}_\odot$, where all field lines are open. The heliocentric current sheet (HCS) location is indicated by the minimum of the speed curve.

can we say something without having traced the lines? NOTE: (by ALBERT) Todo el punto de la última Figura es precisamente decir algo. La comparación con la Figura 10 muestra una anti-correlación entre la densidad basal de DEMT y la velocidad terminal de AWSoM.

For each rotation, everything to the south of the HCS maps down to the southern open region in the Figures 11, and the same for the northern hemisphere, showing an anti-correlation between N_e at low heights and high V_r at $6\,\mathrm{R}_\odot$.

Voy a intentar jugar con las lineas tipo 3 aumentando su cota inferior de latitud para ver si los histogramas de temp media dejan de ser tan dispersos y se vuelven mas sub-1MK.

4. Discussion

NOTE: (by Albert) This section will discuss and summarize some main conclusions, possibly in three groups: a) DEMT analysis alone (including thermodynamical structure, up/down loops, energy considerations, etc.), b) Comparison AWSoM/DEMT (longitude-averaged latitudinal profiles, height-dependence profiles in different magnetic structures, etc), and c) Correlation betweem AWSoM terminal wind speed and DEMT basal density, I will expand on this later this week as this may require help from Michigan).

NOTE: Here is a paragraph describing the empirical successes in the reconstruction of both rotations.

Table 2. Median value (indicated as "Md") of the statistical distribution of N_{CB}, λ_N, and $\langle T_{\mathrm{m}} \rangle$ for each coronal type of lines defined in Section 2.3. DEMT values are expressed in absolute terms, while AWSoM results are informed as a percentual variation relative to the corresponding DEMT value. Propongo que para todas las cantidades absolutas informes siempre dos cifras significativas, y que todos los porcentajes los redondees a cero decimales (o sea, a veces una y a veces dos cifras significativas) y que no uses puntos para estos nunca. Ejemplo para CR-2082 N_{CB} de Type-II: 1.0 (−23%). Ejemplo para CR-2208 λ_N de Type-II: 12.0 (−17%). Ejemplo para CR-2208 $\langle T_{\mathrm{m}} \rangle$ de Type-II: 1.6 (−10%).

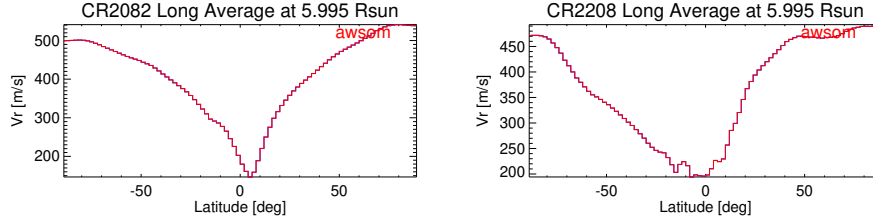| Type	Md(N_{CB}) [$10^8\,\mathrm{cm}^{-3}$]	Md(λ_N) [$10^{-2}\,\mathrm{R_\odot}$]	Md($\langle T_{\mathrm{m}} \rangle$) [MK]
CR-2082			
I	1.13 (−11.9%)	8.3 (− 2.4%)	1.29 (−10.8%)
II	0.97 (−22.5%)	8.9 (+ 2.2%)	1.33 (− 4.5%)
III	0.66 (−16.8%)	7.7 (− 9.1%)	0.98 (− 9.2%)
CR-2208			
I	0.97 (+ 9.3%)	9.8 (− 7.1%)	1.55 (−14.2%)
II	0.77 (+11.7%)	11.6 (−17.2%)	1.55 (− 9.7%)
III	0.56 (− 1.9%)	8.6 (−16.3%)	1.04 (− 9.6%)

Figure 15. Longitude-averaged latitudinal dependence of the AWSoM model wind speed at $6.0\,\mathrm{R_\odot}$ for CR2082 (left panel) and CR2208 (right panel). NOTE: (by Albert): Even if this is not yet the terminal speed, it is a pretty high height, and one can already see the transition from FAST to SLOW speed in the model, where the absolute minimum indicates the location of the HCS at this height. I believe it is interesting to compare these two curves with Figure 10. Note that while in this Figure all latitudes are magnetically open, in Figure 10 only the part at latitudes larger than the vertical black lines are open. Note that DEMT shows that in the open low corona N_e decreases from the O/C boundary towards the poles, anti-correlating with the AWSoM terminal speed, which is nice. In order to quantify this anti-correlation we need to trace the terminal speed and the DEMT N_e, which we may need to do with the help of Chip and Nishtha. Chip, we can discuss this idea over Skype after Xmas if you are around.

*In comparing the DEMT results obtained for the two selected targets, it is important to bear in mind they rely on data provided by two different instruments: AIA and EUVI. In order to quantify the systematic difference of the DEMT products based on both instruments, Nuevo *et al.* (2015), who were the first to apply DEMT to AIA data, analyzed a single target using both instruments independently. They found that while the density product is essentially

equal, the temperature product of DEMT based on AIA data is systematically 8% larger than the one based on EUVI data, i.e. $T_{\mathrm{m}}^{\mathrm{(AIA)}}/T_{\mathrm{m}}^{\mathrm{(EUVI)}} \approx 1.08$. Considering such correction, Figure 6 and Table 1 indicate that CR-2208 was $\approx 10-15\%$ hotter than CR-2082 throughout the streamer belt region. As for the electron density products, CR-2208 was found to be $\approx 15-20\%$ less dense than CR-2082 throughout the streamer belt region. These systematic differences are beyond the uncertainty level in the DEMT products due to systematic sources (radiometric calibration and tomographic regularization), that Lloveras *et al.* (2017) estimated to be $\lesssim 5\%$ and $\approx 2\%$ for the electron temperature and density, respectively.

*Coronal magnetic structures for which the temperature increases/decreases with height in the range of heights covered by DEMT, $1.02–1.22\,\mathrm{R}_\odot$, have been dubbed as "up"/"down" loops by Huang *et al.* (2012) and Nuevo *et al.* (2013), who first observed their presence by means of DEMT. As speculated by the authors of those works, loops of type down can be expected if the heating deposition is strongly confined near the coronal base of a magnetic loop. Down loops were first predicted by Serio *et al.* (1981), and later on by Aschwanden and Schrijver (2002). In a recent study by Schiff and Cranmer (2016), down and up loops have been successfully reproduced by a numerical implementation of a 1D steady-state model that considers time-averaged heating rates.

We found down legs in the DEMT reconstructions mainly in the equatorial latitudes, being a greater quantity and better distribution along longitudes in CR-2082 than in CR-2208. Nuevo *et al.* (2013) showed a decrease in the amount of down loops as the solar activity increases, which is consistent with the results shown in this article.

*We can see, on type 0 loops, a median value of energy input flux (ϕ_h) for CR-2082 twice bigger than CR-2208. In both rotations this magnitude has negative values, this can refer to some loops where loop-integrated radiative flux ϕ_r) is too small in comparison with the larger gradients of negative conductive flux ϕ_c), resulting in negative energy input flux.

This effect can be due a subestimation of the density present in the loop or the limited range of temperature used to reconstruct tomographic parameters, that can affect the compute of radiative power. Nevertheless, this population represent lower than the ALGÚN PORCENTAJE% of total population in both cases.

Consistent that the density in CR-2082 was higher, the ϕ_r was also higher. In both rotations the magnitudes in the temperature gradients are similar, but the temperatures in CR-2208 were consistently higher at all heights, resulting in a larger ϕ_c in module. This results are in agree with the observations of Mac Cormack *et al.* (2017).

THE AR of CR-2082 wasn't well modeled by AWSoM.

In both rotations, AWSoM and DEMT resutls shows same termodynamic structures along latitude and longitude with very comparable values between $1.055-1.25\,\mathrm{R}_\odot$

Figure 13 and Table 2 indicate that AWSoM reconstruction of CR-2082 was found to be less dense $\approx 11-22\%$ and colder $\approx 5-10\%$.

Both reconstructions of CR-2208 reconstructed the ARs with very similare values and in almost the same latitude-longitude location. Figure 14 and Table 2 indicate that AWSoM reconstruction of CR-2208 was found to be denser $\approx 0 - 10\%$ and colder $\approx 10 - 15\%$.

CR-2208 was $\approx 10 - 15\%$ hotter than CR-2082 throughout the streamer belt region. As for the electron density products, CR-2208 was found to be $\approx 15 - 20\%$ less dense than CR-2082 throughout the streamer belt region. These systematic differences are beyond the uncertainty level in the DEMT products due to systematic sources (radiometric calibration and tomographic regularization), that Lloveras *et al.* (2017) estimated to be $\lesssim 5\%$ and $\approx 2\%$ for the electron temperature and density, respectively.

I would like to say something about FIgure 10. Maybe the weird tale in AWSoM Ne in the poles. Ideas?

References

Aschwanden, M.J.: 2004, *Physics of the Solar Corona. An Introduction*, Praxis Publishing Ltd, ??? ADS.

Aschwanden, M.J., Schrijver, C.J.: 2002, Analytical Approximations to Hydrostatic Solutions and Scaling Laws of Coronal Loops. *Astrophys. J. Suppl.* **142**(2), 269. DOI. ADS.

Del Zanna, G., Dere, K.P., Young, P.R., Landi, E., Mason, H.E.: 2015, CHIANTI - An atomic database for emission lines. Version 8. *Astron. Astrophys.* **582**, A56. DOI. ADS.

Frazin, R.A.: 2000, Tomography of the Solar Corona. I. A Robust, Regularized, Positive Estimation Method. *Astrophys. J.* **530**, 1026. DOI. ADS.

Frazin, R.A., Vásquez, A.M., Kamalabadi, F.: 2009, Quantitative, Three-dimensional Analysis of the Global Corona with Multi-spacecraft Differential Emission Measure Tomography. *Astrophys. J.* **701**, 547. DOI. ADS.

Huang, Z., Frazin, R.A., Landi, E., Manchester, W.B., Vásquez, A.M., Gombosi, T.I.: 2012, Newly Discovered Global Temperature Structures in the Quiet Sun at Solar Minimum. *Astrophys. J.* **755**, 86. DOI. ADS.

Lloveras, D.G., Vásquez, A.M., Nuevo, F.A., Frazin, R.A.: 2017, Comparative Study of the Three-Dimensional Thermodynamical Structure of the Inner Corona of Solar Minimum Carrington Rotations 1915 and 2081. *Solar Phys.* **292**(10), 153. DOI. https://doi.org/10.1007/s11207-017-1179-z.

Mac Cormack, C., Vásquez, A.M., López Fuentes, M., Nuevo, F.A., Landi, E., Frazin, R.A.: 2017, Energy Input Flux in the Global Quiet-Sun Corona. *Astrophys. J.* **843**, 70. DOI. ADS.

Nuevo, F.A., Huang, Z., Frazin, R., Manchester, i. Ward B., Jin, M., Vásquez, A.M.: 2013, Evolution of the Global Temperature Structure of the Solar Corona during the Minimum between Solar Cycles 23 and 24. *Astrophys. J.* **773**(1), 9. DOI. ADS.

Nuevo, F.A., Vásquez, A.M., Landi, E., Frazin, R.: 2015, Multimodal Differential Emission Measure in the Solar Corona. *Astrophys. J.* **811**(2), 128. DOI. ADS.

Press, W.H., Teukolsky, S.A., Vetterling, W.T., Flannery, B.P.: 2002, *Numerical recipes in C++ : the art of scientific computing.* ADS.

Schiff, A.J., Cranmer, S.R.: 2016, Explaining Inverted-temperature Loops in the Quiet Solar Corona with Magnetohydrodynamic Wave-mode Conversion. *Astrophys. J.* **831**(1), 10. DOI. ADS.

Serio, S., Peres, G., Vaiana, G.S., Golub, L., Rosner, R.: 1981, Closed coronal structures. II - Generalized hydrostatic model. *Astrophys. J.* **243**, 288. DOI. ADS.

Spitzer, L.: 1962, *Physics of Fully Ionized Gases.* ADS.

Vásquez, A.M.: 2016, Seeing the solar corona in three dimensions. *Advances in Space Research* **57**, 1286. DOI.